coatings

MDPI

Article

Conductive Carbon-Wrapped Fluorinated Hard Carbon Composite as High-Performance Cathode for Primary Lithium Batteries

Nange Chen [1,2,3], Guanjun Zhang [4], Huixin Chen [2,3,*] and Hongjun Yue [2,3,*]

[1] College of Chemistry, Fuzhou University, Fuzhou 350108, China
[2] CAS Key Laboratory of Design and Assembly of Functional Nanostructures, Fujian Provincial Key Laboratory of Nanomaterials, Fujian Institute of Research on the Structure of Matter, Chinese Academy of Sciences, Fuzhou 350002, China
[3] Xiamen Key Laboratory of Rare Earth Photoelectric Functional Materials, Xiamen Institute of Rare Earth Materials, Haixi Institutes, Chinese Academy of Sciences, Xiamen 361021, China
[4] Tianjin Lantian Special Power Supply Science and Technology Joint-Stock Co., Tianjin 300393, China
* Correspondence: chenhuixin@fjirsm.ac.cn (H.C.); hjyue@fjirsm.ac.cn (H.Y.)

Abstract: Lithium/carbon fluoride (Li/CF_x) batteries have been widely researched due to their high theoretical specific energy. To create a high-performance electrode, the fluorinated hard carbon (FHC) is prepared by direct gas-phase fluorination. It has a high F/C ratio of 0.95 based on the gravimetric method. Selecting hard carbon (HC) with a high surface area as the carbon source allows for FHC to achieve suitable interlayer spacing and specific surface area, as well as abundant pore structures to facilitate rapid lithium ion transportation. Additionally, a composite of graphene and carbon nanotubes (CNTs) is coated on the surface of FHC, enhancing electron transport speed. The resulting FHC&C exhibits a very high energy density of 1256 Wh kg^{-1} and an excellent power density of 72,929 W kg^{-1} at a high rate of 40 C. Moreover, compared to commercial CF_x, FHC&C exhibits higher energy and power densities, thus presenting a promising practical application prospect.

Keywords: carbon fluoride; hard carbon; composite; primary lithium battery

Citation: Chen, N.; Zhang, G.; Chen, H.; Yue, H. Conductive Carbon-Wrapped Fluorinated Hard Carbon Composite as High-Performance Cathode for Primary Lithium Batteries. *Coatings* **2023**, *13*, 812. https://doi.org/10.3390/coatings13050812

Academic Editor: Ajay Vikram Singh

Received: 26 March 2023
Revised: 13 April 2023
Accepted: 20 April 2023
Published: 22 April 2023

1. Introduction

The superiority of Li/CF_x batteries lies in their remarkable theoretical energy density (2189 Wh kg^{-1}), which is higher when compared to other primary lithium batteries, including Li/MnO_2, Li/$SOCl_2$, and Li/SO_2 batteries [1,2]. Therefore, Li/CF_x batteries are widely employed in various fields, such as the military, aerospace, and medical industries [3,4]. The carbon source plays a critical role in the preparation of CF_x [5]. Graphite fluoride exhibits poor electronic conductivity, which leads to unsatisfactory rate performance of Li/CF_x batteries [6–8]. Consequently, researchers are exploring alternatives to graphite fluoride and have been investigating the potential utility of low-cost and scalable amorphous carbons such as hard carbon (HC) and soft carbon (SC) as carbon sources for commercial CF_x [9,10]. Other different types of carbon, including graphene [11], graphene-oxide [12], fullerenes [13], carbon nanotubes(CNTs) [14,15], carbon nanofibers [16], mesoporous carbon [17], nanostructured carbon nanodiscs [18], and calcinated macadamia nut shell [19], have also been fluorinated through various methods.

The other key factor determining the performance of CF_x is the fluorination condition, in addition to the carbon source [5]. The most conventional method of fluorination is direct gas-phase fluorination, which involves the reaction of flowing fluorine gas and carbon in heated tubes [20]. This method is easy to scale up and enables the preparation of highly fluorinated CF_x [21].

Creating composite cathodes with highly conductive materials can improve conductivity and achieve a better electrochemical performance of CF_x [22]. For example, polypyrrole

(PPy) was coated on the surface of CF_x to enhance the rate capability [23,24]. In addition, carbon-based materials, such as carbon black, graphene, and multi-walled carbon nanotubes (MWCNTs), have been used to prepare composite cathodes [25,26]. The addition of MWCNTs achieved a 26% increase in capacity than acetylene black with the same quality at a rate of 1 C [25]. Moreover, a very thin layer of carbon coatings on the surface of CF_x was formed by heat treatment method at 600 °C in nitrogen for 2 h, and the cells using carbon-coated CF_x cathode had higher energy and power densities [27].

In this study, a fluorinated hard carbon (FHC) was prepared by direct gas-phase fluorination of the HC with a high surface area and was then modified by coating conductive carbon to obtain the fluorinated hard carbon/carbon composite (FHC&C) cathode. FHC&C exhibits high energy densities (2371 Wh kg^{-1} at 0.01 C, 1764 Wh kg^{-1} at 8 C, and 1256 Wh kg^{-1} at 40 C, 1 C = 800 mA g^{-1}) and power densities (72,929 W kg^{-1} at 40 C), superior to the commercial CF_x obtained from Japan (Daikin). These results indicated that FHC&C has the potential to be used in various applications and promote the development of Li/CF_x batteries.

2. Experimental Section

2.1. Materials Synthesis

Figure 1a describes the brief process of the FHC&C preparation. The HC was supplied by Beijing Ainengju Technology Co., Ltd (Beijing, China). This material uses biomass coconut endocarp as the precursor and is prepared by carbonization, activation, acid washing, and other treatments. It was fluorinated by direct gas-phase fluorination method at 360, 380, and 400 °C for 12 h, as described in the previous work [21]. The conductive carbon paste was purchased from The Sixth Element Materials Technology Co., Ltd. (Changzhou, China). It consists of graphene, CNTs, solvent, and little dispersant. The conductive carbon and FHC were evenly dispersed in deionized water by sonication and agitation for 3 h. After that, the mixture was filtered and dried by freeze-drying to obtain FHC&C powders. The proportion of conductive carbon was 0.5 wt.%, 1 wt.%, and 2 wt.%.

2.2. Materials Characterization

X-ray diffraction (XRD), scanning electron microscope (SEM), transmission electron microscopy (TEM), Brunauer–Emmett–Teller (BET) thermogravimetric (TGA), Fourier transform infrared spectroscopy (FT-IR), and X-ray photoelectron spectroscopy (XPS) were used to analyze the physical characterization of samples. The instrument information and detailed parameters are presented in the Supplementary Materials.

2.3. Electrochemical Measurements

The cathode was prepared by spreading a slurry of 80 wt.% CF_x, 10 wt.% carbon black, and 10 wt.% Carboxymethylcellulose sodium (CMC) in deionized water on Al foil. The electrodes were dried in a vacuum oven at 80 °C for 6 h to remove the solvent and were cut into 14 mm discs with an active material loading of around 0.7 mg cm^{-2}. Coin cells (CR2016) were assembled with lithium metal as the counter electrode, 1.0 M $LiBF_4$ in ethylene carbonate (EC)/dimethyl carbonate (DMC)/ethyl methyl carbonate (EMC) as the electrolyte (volume ratio = 1:1:1), and Celgard 2500 as the separators in an argon-filled glove box (H_2O < 0.1 ppm, O_2 < 0.1 ppm). Discharge tests were carried out on a Neware battery test system at 25 °C and -20 °C, and the cut-off voltage was 1.5 V.

The detailed parameters of the galvanostatic intermittent titration technique (GITT) and electrochemical impedance spectroscopy (EIS) are presented in the Supplementary Materials.

3. Results and Discussions

The fluorine content in fluorinated carbon has a significant effect on its electrochemical performance. Specifically, a low fluorine content is associated with a good power density but relatively low-capacity density, whereas a high fluorine content tends to improve

capacity density at the expense of power density [21]. In our study, we controlled the F content by adjusting the temperatures of fluorination. According to the gravimetric method, the F/C ratios of FHC samples obtained at fluorination temperatures of 360, 380, and 400 °C were equal to 0.85, 0.95, and 1.10, respectively. As shown in Figure S1, FHC-0.95 exhibited the highest energy densities of the three materials.

As shown in Figure 1a, FHC was synthesized by gas-phase fluorination of HC and formed FHC&C composites together with conductive carbon. The addition of a small amount of graphene (<2 wt.%) can increase capacity while also preventing the undesirable voltage polarization effect that can occur with higher graphene percentages in cathodes [28]. High carbon content impedes the diffusion of Li^+ by lengthening the diffusion path [29]. The discharge performance of Li/CF_x batteries is determined by lithium-ion diffusion when the discharge rate becomes higher [25]. As shown in Figure S2, our work reached similar conclusions, and FHC&C-1.0% provided the highest specific capacities. FHC&C in this paper refers to FHC&C-1%.

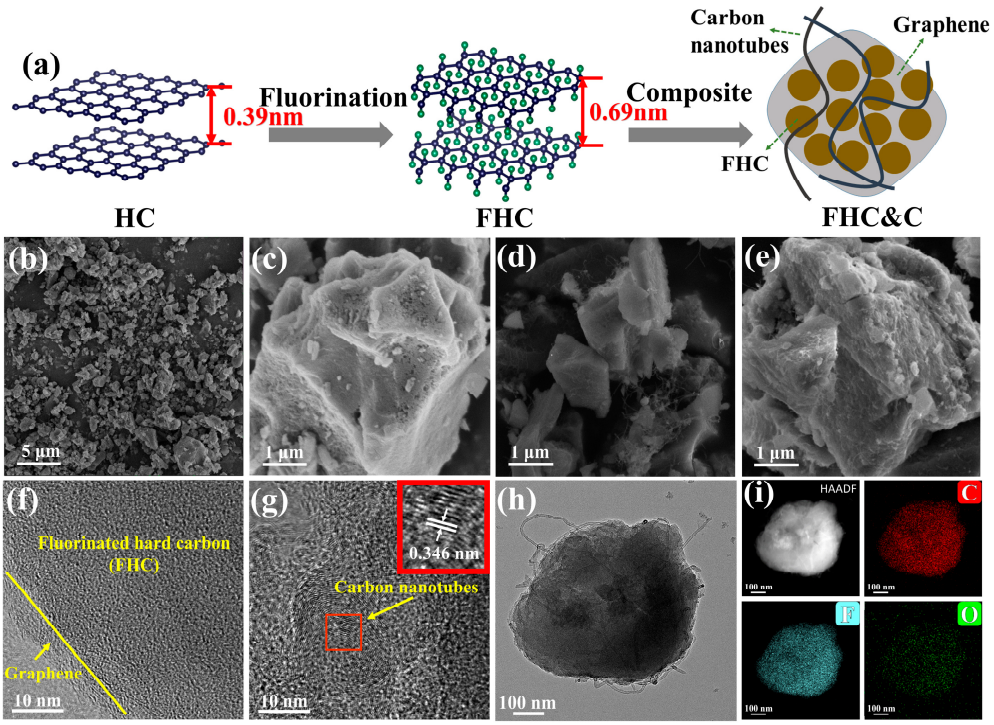

Figure 1. (**a**) Schematic illustration of the synthesis process; (**b**,**c**) SEM images of FHC and (**d**,**e**) FHC&C; (**f**,**g**) TEM images of FHC&C; (**h**,**i**) Elemental mapping images of FHC&C.

Figure 1b,c present a smoother surface of FHC (compared to the HC in Figure S3) and clear pores etched by the F_2. As shown in Figure 1d,e, FHC is coated with graphene and wrapped by CNTs akin to cobweb. Graphene/CNTs composite forms a "dot-line-surface" three-dimensional conductive network on the surface of FHC, which enables faster electron transport [30]. The TEM image of FHC&C (Figure 1f) displayed a layer of about 2–3 nm thick graphene on the surface that has different orientations from FHC. CNTs are clearly observed at the edge of the particle (Figure 1h) and the interlayer spacing is measured to be 0.346 nm (Figure 1g). Figure 1i provided the high-angle annular dark-field (HAADF-STEM) image and the corresponding C, F and O elements mapping, revealing a low presence of O element and the uniform fluorination of the sample.

The BET method was employed to analyze the surface structures, which revealed specific surface areas of 1693, 171, 524, and 536 $m^2\ g^{-1}$ for HC, Daikin, FHC, and FHC&C, respectively. The specific surface areas of FHC&C and FHC were larger than those of most CF_x reported in the literature (Table S2). The Nitrogen adsorption and desorption isotherm of HC (Figure S4b) is a type I(b) curve. The gas adsorption volume in the low-pressure

range rose rapidly and then remained stable. It indicated the existence of micropores less than 2.5 nm, which aligned with the results depicted in Figure S4c. The Nitrogen adsorption–desorption isotherms of FHC (Figure S5a) and FHC&C (Figure 2a) are type IV(a) curves with H4-type hysteresis loops, indicating the presence of micropores and mesopores. The Pore size distributions of HC and FHC are shown in Figures S4c and S5b. After fluorination, mesopores emerged, and there was a significant reduction in the specific surface area and the number of micropores. This was due to the collapse of the pore structure and the impact of F_2 gas on the sample during fluorination. The specific surface area, nitrogen adsorption–desorption curve, and pore size distribution of FHC&C were similar to FHC, indicating that the modification had little effect on the crystal structure of the material. As shown in Figure 2b, FHC&C possessed mesoporous (2.35 nm, 3.20 nm, and 7.069 nm) and microporous (0.59 nm and 1.05 nm), while Daikin only possessed mesoporous (0.57 nm and 0.89 nm). FHC&C had a larger specific surface area and more pores in contrast to Daikin.

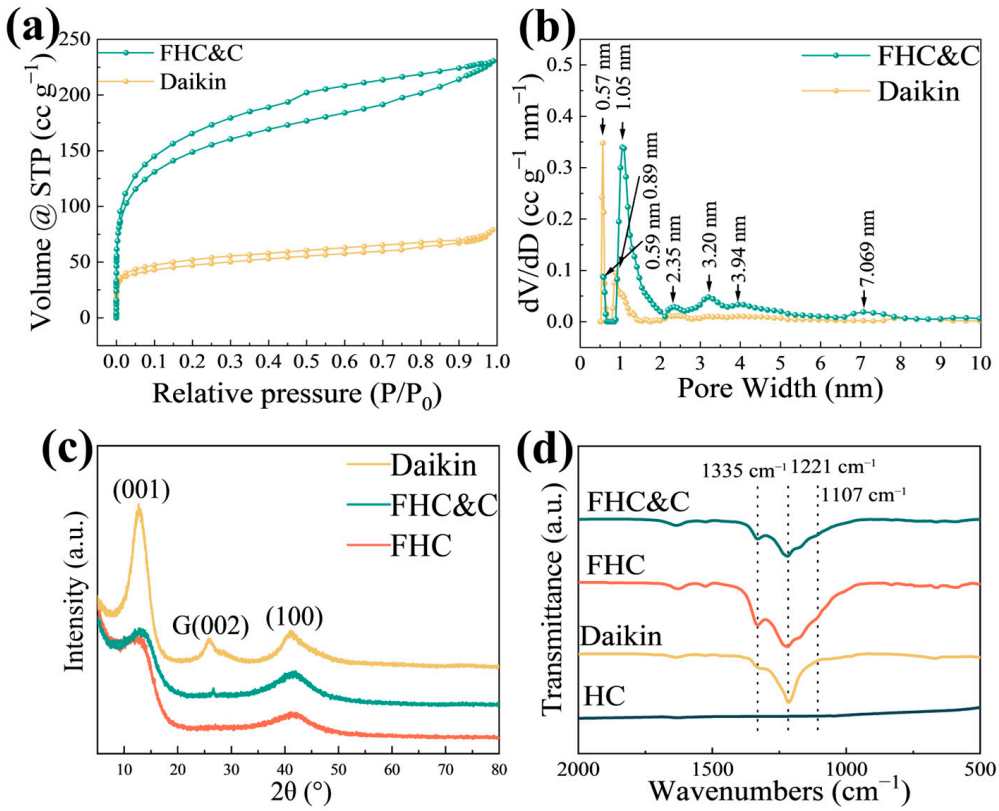

Figure 2. (**a**) Nitrogen adsorption–desorption isotherm and (**b**) Pore size distribution of FHC&C and Daikin; (**c**) XRD patterns of FHC, FHC&C, and Daikin; (**d**) FT-IR spectra of FHC, FHC&C, Daikin, and HC.

The XRD patterns of FHC, FHC&C, Daikin, and HC are presented in Figures 2c and S4. Two broad diffraction peaks of 22.8°and 43.8° corresponding to the interlayer (002) and intra-layer (100) reflections were observed in the XRD pattern of HC, consistent with highly disordered carbon [31]. The peaks at 12.8° and 41.1° of FHC, FHC&C, and Daikin were assigned to the (001) and (100) reflections [32]. The XRD pattern of FHC was close to that of FHC&C except for the peak at around 26.6°, which was assigned to the (002) reflection of the graphene structure [24]. The interlayer distance plays a crucial role in the rate capability of CF_x [33]. According to the XRD patterns, the interlayer distances of HC and FHC derived from the (001) diffraction angles were calculated to be around 0.39 and 0.69 nm by Bragg's equation, respectively [34,35]. The interlayer spacing of HC was larger than 0.37 nm, which was consistent with typical hard carbon (Figure S4a) [36].

In addition, the interlayer spacing increased after fluorination due to the intercalation of adjacent interlayers by fluorine atoms.

FT-IR analysis was employed to examine the chemical bonds of materials (Figure 2d). The peak at 1700 cm^{-1} was attributed to water absorption by KBr absorbing water, and HC did not have any other peaks. The peaks at the wavenumber of 1335 and 1221 cm^{-1} corresponded to the stretching vibration of CF_2 groups and the stretching vibration of covalent C–F bonds, respectively [37]. In addition, the peak at the wavenumber of 1107 cm^{-1} corresponded to the stretching vibration of semi-ionic C–F bonds, which was observed in FHC and FHC&C but not detected in Daikin.

The TGA curves of FHC&C and Daikin under an argon atmosphere are shown in Figure S6. The weight of FHC&C decreased gradually between 300 °C and 500 °C. In this process, defluorination occurred in FHC&C, which indicated that the thermal stability of FHC&C was worse than that of Daikin [38]. At temperatures between 500 and 630 °C, FHC&C and Daikin underwent significant weight loss, indicating their decomposition. During this process, CF_4 and C_2F_4 were the primary volatile products formed through a radical fluorocarbon process [39].

The state of chemical bonds on the sample surface was further analyzed by the XPS technique. Table S1 lists the peak position and assignments of chemical bonds in the XPS spectrum [8,40–42]. From the XPS survey spectrum (Figure 3a–c), it could be seen that the three samples were mainly composed of C and F elements. Figure 3d shows four peaks in the C 1*s* spectrum of FHC, which are C–C (~284.8 eV), C–C (~287.3 eV), covalent C–F (~290.0 eV), and CF_2 (~ 292.0 eV). Figure 3e shows that FHC&C also has four peaks similar to FHC, which are C–C (~284.8 eV), C–C (~287.0 eV), covalent C–F (~289.8 eV), and CF_2 (~ 291.8 eV). After modification, the peak area representing the C–C bonds increased due to the existence of the conductive carbon on the surface of FHC&C. Figure 3f shows five peaks on the C 1*s* spectrum of Daikin, which are C–C (~284.8 eV), C–C (~286.8 eV), covalent C–F (~290.0 eV), CF_2 (~291.6 eV), and CF_3 (~295.0 eV). The peak areas for C–C bonds and C–C bonds in FHC and FHC&C were larger than those in Daikin, and these conductive bonds could accelerate electron transfer and enhance rate discharge performance [43,44]. Figure 3g–i shows the F 1*s* peaks of FHC, FHC&C, and Daikin at 689.0 eV, 688.4 eV, and 688.7 eV, respectively. The F 1*s* peaks of covalent bonds, half-ionic bonds, and semi-ionic bonds were at 689.8 eV, 688.2 eV, and 685.9 eV. The small shift of approximately 0.6 eV from FHC to FHC&C suggested that the modification weakened C–F bonds [45].

Figure 4 shows the galvanostatic discharge curves of FHC, FHC&C, and Daikin samples. To comprehensively study the rate performance of the material, we used six different current densities during the discharge process. It could be observed that the discharge voltage plateau and the specific capacity decreased with the increase of the discharge current. The voltages of FHC and FHC&C were unstable and gradually dropped during the discharge process. The initial discharge voltage of FHC at 0.01 C was above 3.2 V, and the discharge-specific capacity was as high as 800 mA h g^{-1}. Compared with FHC, the rate performance of FHC&C was significantly improved, and the discharge-specific capacities were apparently improved, especially at high rates. The specific capacities of FHC&C were 830 mA h g^{-1} at 0.01 C and 545 mA h g^{-1} at 40 C. After modification, the voltage hysteresis was improved, and the discharge-specific capacities increased. At 0.01 C, Daikin exhibited a specific capacity of 905 mA h g^{-1} with a discharge voltage plateau of 2.7 V, while at 40 C, it exhibited a specific capacity of 632 mA h g^{-1} with a discharge voltage plateau of 1.9 V. The discharge curve of Daikin exhibited smooth but lower discharge voltage plateaus and higher discharge capacity (Figure 4c), which are the typical discharge curve characteristics of fluorinated graphite [46].

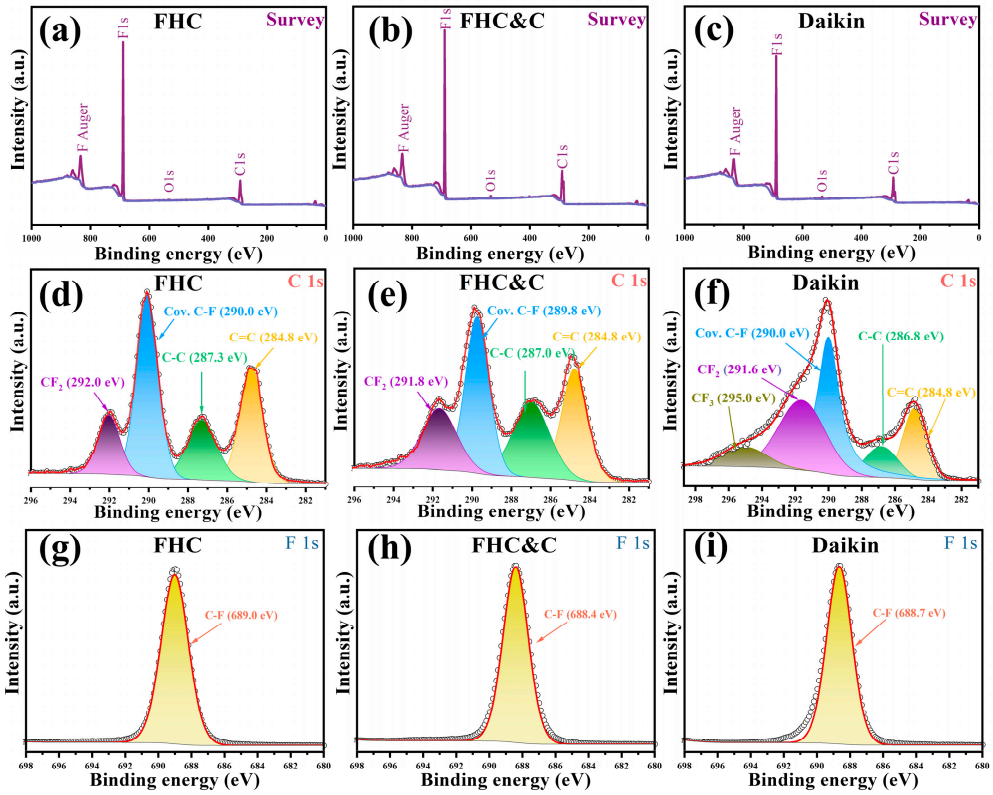

Figure 3. The XPS survey spectra for (**a**) FHC, (**b**) FHC&C, and (**c**) Daikin; the C 1*s* spectra of (**d**) FHC, (**e**) FHC&C, and (**f**) Daikin; the F 1*s* spectra of (**g**) FHC, (**h**) FHC&C, and (**i**) Daikin.

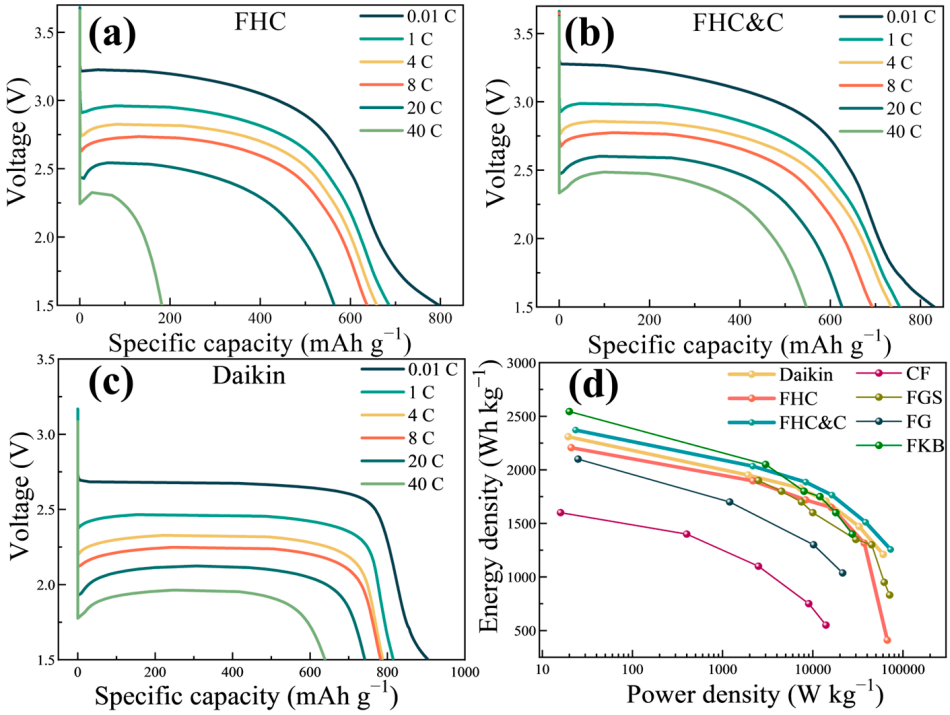

Figure 4. Galvanostatic discharge curves of (**a**) FHC, (**b**) FHC&C, and (**c**) Daikin were obtained at different current densities; (**d**) Ragone plots of FHC, FHC&C, and Daikin, and CF_x-based cathodes in other literature, in which CF, FGS, FG, and FKB represent fluorinated natural graphite, fluorinated graphene microspheres, fluorination reduced graphene oxide, and fluorinated Ketjenblack, respectively.

For an intuitive comparison of the power density and the energy density at different discharge currents, the Ragone plot is shown in Figure 4d. With the increase in discharge rate, the energy density decreased with the increase in power density. FHC&C exhibited an energy density of 2371 Wh kg^{-1} at 0.01 C and a power density of 72,929 W kg^{-1} at 40 C. This material is superior to Daikin, FHC, and most of the CF_x-based materials in the literature. Detailed attribute parameters of various CF_x-based materials are listed in Table S2.

The main reason for the difference in the discharge voltage is the overpotential(η), which includes ohmic polarization, electrochemical polarization, and concentration polarization. Ohmic loss is related to the internal resistance, and the electrochemical polarization is associated with the charge exchange rate. During the discharge process, the products generated by the electrochemical reaction hinder the diffusion of lithium ions, which is the main factor in producing the concentration polarization [7]. Concentration polarization is always the rate-determining step due to sluggish Li^+ transport in the solid state and across the interface [47].

Figure 5a shows the impedance spectra of FHC, FHC&C, and Daikin cells before discharge. The low-frequency region is a sloping line controlled by the diffusion of the electrode process, and the high-frequency region is a circular arc controlled by the electrochemical step [48]. The charge-transfer resistances (R_{ct}) of fitted results are listed in Table S3. FHC&C had the lowest Rct (15.26 Ω), indicating superior conductivity. It was primarily due to the three-dimensional conductive networks formed by the graphene/CNTs composite [49].

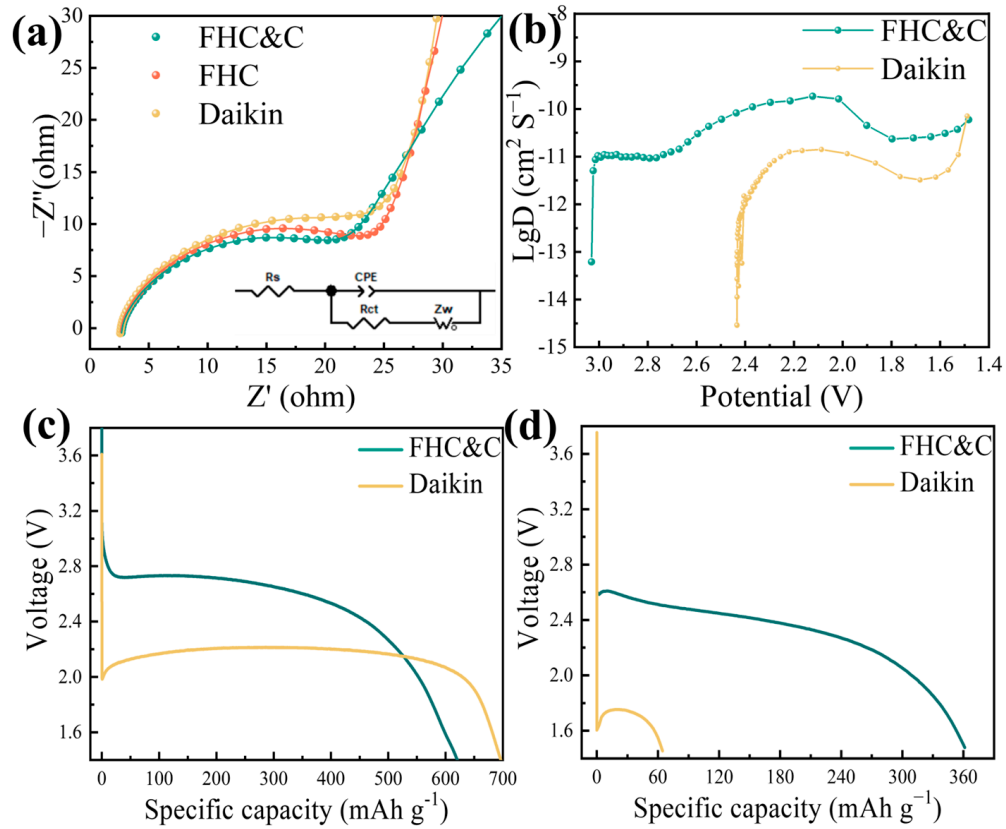

Figure 5. (**a**) Impedance spectra of FHC, FHC&C, and Daikin cells; (**b**) Li^+ diffusion coefficient estimated by GITT; Galvanostatic discharge curves of Daikin and FHC&C at −20 °C at the rates of (**c**) 0.1 C and (**d**) 1 C.

Based on the above discussion, concentration polarization is another factor that affects the discharge voltage. We measured the Li^+ diffusion coefficient (D_{Li+}) by the GITT method.

D_{Li+} was obtained from the potential response to a small constant current pulse I_p via the following formula [50]:

$$D_{Li+} = \frac{4}{\pi\tau}\left(\frac{m_B V_M}{M_B S}\right)^2\left(\frac{\Delta Es}{\Delta Et}\right)^2$$

Figure 5b shows the gradual change of the D_{Li+} value during the discharge process. Initially, the increase in D_{Li+} value was due to the consumption of C–F bonds and the formation of carbon [44]. At a voltage range of 2.1 V to 1.7 V, the surface of the particles was gradually saturated with LiF, which hindered the ion transmission, reflected in the decrease of the D_{Li+} value [51]. At a voltage range of 1.7 V to 1.5 V, the D_{Li+} value increased again, probably due to the formation of Li_2F [19]. Compared with Daikin, FHC&C had a higher lithium ion diffusion capacity, which explained the high discharge voltage behavior [52].

As shown in Figure 5c,d, at a low temperature (−20 °C), the discharge voltage of the battery decreased, so the advantages of FHC&C were further enhanced. At a rate of 0.1 C, the energy density of FHC&C was 1632 Wh kg^{-1}, while that of Daikin was 1475 Wh kg^{-1}. As the discharge rate escalated to 1 C, the contrast between the two cells became more apparent. FHC&C maintained a capacity of 360 mA h g^{-1} and an energy density of 827 Wh kg^{-1}, whereas Daikin lost discharge ability.

4. Conclusions

In summary, our study involved the synthesis of FHC&C followed by their thorough investigation using physical and electrochemical methods. Selecting a suitable hard carbon as the carbon source, we were able to produce FHC with a large layer spacing, high specific surface area, and abundant pores. These physical properties were found to greatly enhance lithium ion transport, leading to faster reaction kinetics. In addition, the composite of graphene/CNTs established three-dimensional conductive networks that further improved the conductivity of FHC&C. As a result of these features, our study found that FHC&C has better energy densities and power densities than the advanced commercial CF_x, making it promising for practical applications.

Supplementary Materials: The following supporting information can be downloaded at: https://www.mdpi.com/article/10.3390/coatings13050812/s1, Figure S1. Galvanostatic discharge curves of FHC (fluorinated hard carbon) with different F/C ratio of (a) 0.85, (b) 0.95, and (c) 1.10; Figure S2. Galvanostatic discharge curves of FHC (fluorinated hard carbon) and FHC&C (fluorinated hard carbon/carbon composite) with different conductive carbon contents; Figure S3. SEM images of HC (hard carbon); Figure S4. (a) XRD patterns, (b) Nitrogen adsorption-desorption isotherm, and (c) Pore size distribution of HC; Figure S5. (a) Nitrogen adsorption-desorption isotherm, and (b) Pore size distribution of FHC; Figure S6. TGA of FHC&C and Daikin; Table S1. Peaks assignments and proportions from the XPS spectra; Table S2. In comparison with the results in this work, a summary of the electrochemical performance of. Li/CFx cathode materials in the literatures; Table S3. The resistance values of Daikin, FHC, and FHC&C fitted from the equivalent circuit of EIS.

Author Contributions: Data curation and writing—original draft, N.C.; formal analysis, N.C. and G.Z.; validation, G.Z.; conceptualization, methodology, writing—review and editing H.C.; resources, H.C. and H.Y.; Supervision, H.Y. All authors have read and agreed to the published version of the manuscript.

Funding: This work was financially supported by the Fujian Science and Technology Planning Projects of China (Grant No. 2022T3067), and the Science and Technology Planning Program of Xiamen (Grant No. 2022CXY0701).

Institutional Review Board Statement: Not applicable.

Informed Consent Statement: Not applicable.

Data Availability Statement: Not applicable.

Conflicts of Interest: The authors declare no conflict of interest.

References

1. Fang, Z.; Peng, Y.; Zhou, X.; Zhu, L.; Wang, Y.; Dong, X.; Xia, Y. Fluorinated carbon materials and the applications in energy storage systems. *ACS Appl. Energy Mater.* **2022**, *5*, 3966–3978. [CrossRef]
2. Jiang, J.; Ji, H.N.; Chen, P.Y.; Ouyang, C.Y.; Niu, X.B.; Li, H.; Wang, L.P. The influence of electrolyte concentration and solvent on operational voltage of Li/CF_x primary batteries elucidated by Nernst Equation. *J. Power Sources* **2022**, *527*, 7. [CrossRef]
3. Orenstein, J. Electrons pair themselves. *Nature* **1999**, *401*, 333–335. [CrossRef] [PubMed]
4. Jones, J.-P.; Smart, M.C.; Krause, F.C.; West, W.C.; Brandon, E.J. Batteries for robotic spacecraft. *Joule* **2022**, *6*, 923–928. [CrossRef]
5. Liu, Y.; Jiang, L.; Wang, H.; Wang, H.; Jiao, W.; Chen, G.; Zhang, P.; Hui, D.; Jian, X. A brief review for fluorinated carbon: Synthesis, properties and applications. *Nanotechnol. Rev.* **2019**, *8*, 573–586. [CrossRef]
6. Lam, P.; Yazami, R. Physical characteristics and rate performance of $(CF_x)_n$ (0.33 < x < 0.66) in lithium batteries. *J. Power Sources* **2006**, *153*, 354–359.
7. Zhang, S.S.; Foster, D.; Wolfenstine, J.; Read, J. Electrochemical characteristic and discharge mechanism of a primary Li/CF_x cell. *J. Power Sources* **2009**, *187*, 233–237. [CrossRef]
8. Yang, X.; Zhang, G.; Bai, B.; Li, Y.; Li, Y.; Yang, Y.; Jian, X.; Wang, X. Fluorinated graphite nanosheets for ultrahigh-capacity lithium primary batteries. *Rare Metals* **2021**, *40*, 1708–1718. [CrossRef]
9. Chen, P.; Wang, B.; Wu, Z.; Niu, X.; Ouyang, C.; Li, H.; Wang, L. Fluorinated soft carbon as ultra–high energy density potassium–ion battery cathode enabled by a ternary phase K_xFC. *J. Energy Chem.* **2022**, *77*, 38–44. [CrossRef]
10. Zhou, R.X.; Li, Y.; Feng, Y.Y.; Peng, C.; Feng, W. The electrochemical performances of fluorinated hard carbon as the cathode of lithium primary batteries. *Compos. Commun.* **2020**, *21*, 100396. [CrossRef]
11. Wang, X.; Dai, Y.; Gao, J.; Huang, J.; Li, B.; Fan, C.; Yang, J.; Liu, X. High-yield production of highly fluorinated graphene by direct heating fluorination of graphene-oxide. *ACS Appl. Mater. Interfaces* **2013**, *5*, 8294–8299. [CrossRef]
12. Damien, D.; Sudeep, P.; Narayanan, T.; Anantharaman, M.; Ajayan, P.; Shaijumon, M. Fluorinated graphene based electrodes for high performance primary lithium batteries. *RSC Adv.* **2013**, *3*, 25702–25706. [CrossRef]
13. Matsuo, Y.; Nakajima, T. Electrochemical properties of fluorinated fullerene C_{60}. *Electrochim. Acta* **1996**, *41*, 15–19. [CrossRef]
14. Adamska, M.; Narkiewicz, U. Fluorination of carbon nanotubes—A review. *J. Fluorine Chem.* **2017**, *200*, 179–189. [CrossRef]
15. Li, Y.; Wu, X.; Liu, C.; Wang, S.; Zhou, P.; Zhou, T.; Miao, Z.; Xing, W.; Zhuo, S.; Zhou, J. Fluorinated multi-walled carbon nanotubes as cathode materials of lithium and sodium primary batteries: Effect of graphitization of carbon nanotubes. *J. Mater. Chem. A* **2019**, *7*, 7128–7137. [CrossRef]
16. Yazami, R.; Hamwi, A.; Guérin, K.; Ozawa, Y.; Dubois, M.; Giraudet, J.; Masin, F. Fluorinated carbon nanofibres for high energy and high power densities primary lithium batteries. *Electrochem. Commun.* **2007**, *9*, 1850–1855. [CrossRef]
17. Fulvio, P.F.; Brown, S.S.; Adcock, J.; Mayes, R.T.; Guo, B.; Sun, X.G.; Mahurin, S.M.; Veith, G.M.; Dai, S. Low-temperature fluorination of soft-templated mesoporous carbons for a high-power lithium/carbon fluoride battery. *Chem. Mater.* **2011**, *23*, 4420–4427. [CrossRef]
18. Ahmad, Y.; Dubois, M.; Guérin, K.; Hamwi, A.; Zhang, W. Pushing the theoretical limit of Li–CF_x batteries using fluorinated nanostructured carbon nanodiscs. *Carbon* **2015**, *94*, 1061–1070. [CrossRef]
19. Peng, C.; Li, Y.; Yao, F.; Fu, H.; Zhou, R.; Feng, Y.; Feng, W. Ultrahigh-energy-density fluorinated calcinated macadamia nut shell cathodes for lithium/fluorinated carbon batteries. *Carbon* **2019**, *153*, 783–791. [CrossRef]
20. Sharma, N.; Dubois, M.; Guerin, K.; Pischedda, V.; Radescu, S. Fluorinated (Nano)Carbons: CF_x Electrodes and CF_x-Based Batteries. *Energy Technol.* **2021**, *9*, 2000605. [CrossRef]
21. Zhong, G.M.; Chen, H.X.; Huang, X.K.; Yue, H.J.; Lu, C.Z. High-Power-Density, High-Energy-Density Fluorinated Graphene for Primary Lithium Batteries. *Front. Chem.* **2018**, *6*, 50. [CrossRef] [PubMed]
22. Wang, D.; Wang, G.X.; Zhang, M.M.; Cui, Y.H.; Yu, J.; Shi, S.Q. Composite cathode materials for next-generation lithium fluorinated carbon primary batteries. *J. Power Sources* **2022**, *541*, 16. [CrossRef]
23. Zhu, L.; Li, L.; Zhou, J.; Pan, Y.; Lei, W.; Ma, Z. Polypyrrole-coated graphite fluorides with high energy and high power densities for Li/CF_x battery. *Int. J. Electrochem. Sci.* **2016**, *11*, 6413–6422. [CrossRef]
24. Groult, H.; Julien, C.; Bahloul, A.; Leclerc, S.; Briot, E.; Mauger, A. Improvements of the electrochemical features of graphite fluorides in primary lithium battery by electrodeposition of polypyrrole. *Electrochem. Commun.* **2011**, *13*, 1074–1076. [CrossRef]
25. Li, Y.; Chen, Y.; Feng, W.; Ding, F.; Liu, X. The improved discharge performance of Li/CF_x batteries by using multi-walled carbon nanotubes as conductive additive. *J. Power Sources* **2011**, *196*, 2246–2250. [CrossRef]
26. Meduri, P.; Chen, H.H.; Xiao, J.; Martinez, J.J.; Carlson, T.; Zhang, J.G.; Deng, Z.D. Tunable electrochemical properties of fluorinated graphene. *J. Mater. Chem. A* **2013**, *1*, 7866–7869. [CrossRef]
27. Zhang, Q.; d'Astorg, S.; Xiao, P.; Zhang, X.; Lu, L. Carbon-coated fluorinated graphite for high energy and high power densities primary lithium batteries. *J. Power Sources* **2010**, *195*, 2914–2917. [CrossRef]
28. Hu, B.L.-H.; Wu, F.-Y.; Lin, C.-T.; Khlobystov, A.N.; Li, L.-J. Graphene-modified $LiFePO_4$ cathode for lithium ion battery beyond theoretical capacity. *Nat. Commun.* **2013**, *4*, 1687. [CrossRef]
29. Yang, S.; Zhao, N.; Dong, H.; Yang, J.; Yue, H. Synthesis and characterization of $LiFePO_4$ cathode material dispersed with nano-structured carbon. *Electrochim. Acta* **2005**, *51*, 166–171. [CrossRef]
30. Wang, C.; Yuan, X.; Tan, H.; Jian, S.; Ma, Z.; Zhao, J.; Wang, X.; Chen, D.; Dong, Y. Three-dimensional carbon-coated $LiFePO_4$ cathode with improved Li-ion battery performance. *Coatings* **2021**, *11*, 1137. [CrossRef]

31. Xiao, L.; Lu, H.; Fang, Y.; Sushko, M.L.; Cao, Y.; Ai, X.; Yang, H.; Liu, J. Low-defect and low-porosity hard carbon with high coulombic efficiency and high capacity for practical sodium ion battery anode. *Adv. Energy Mater.* **2018**, *8*, 1703238. [CrossRef]
32. Root, M.J.; Dumas, R.; Yazami, R.; Hamwi, A. The effect of carbon starting material on carbon fluoride synthesized at room temperature: Characterization and electrochemistry. *J. Electrochem. Soc.* **2001**, *148*, A339–A345. [CrossRef]
33. Li, Y.; Liu, C.; Chen, L.; Wu, X.; Zhou, P.; Shen, X.; Zhou, J. Multi-layered fluorinated graphene cathode materials for lithium and sodium primary batteries. *Rare Met.* **2022**, *42*, 940–953. [CrossRef]
34. Sato, Y.; Itoh, K.; Hagiwara, R.; Fukunaga, T.; Ito, Y. On the so-called "semi-ionic" C–F bond character in fluorine–GIC. *Carbon* **2004**, *42*, 3243–3249. [CrossRef]
35. Ma, J.; Liu, Y.F.; Peng, Y.; Yang, X.X.; Hou, J.; Liu, C.; Fang, Z.W.; Jian, X. UV-radiation inducing strategy to tune fluorinated carbon bonds delivering the high-rate Li/CF_x primary batteries. *Compos. Part B-Eng.* **2022**, *230*, 8. [CrossRef]
36. Xu, B.; Qi, S.; Li, F.; Peng, X.; Cai, J.; Liang, J.; Ma, J. Cotton-derived oxygen/sulfur co-doped hard carbon as advanced anode material for potassium-ion batteries. *Chin. Chem. Lett.* **2020**, *31*, 217–222. [CrossRef]
37. Giraudet, J.; Delabarre, C.; Guérin, K.; Dubois, M.; Masin, F.; Hamwi, A. Comparative performances for primary lithium batteries of some covalent and semi-covalent graphite fluorides. *J. Power Sources* **2006**, *158*, 1365–1372. [CrossRef]
38. Sun, C.; Feng, Y.; Li, Y.; Qin, C.; Zhang, Q.; Feng, W. Solvothermally exfoliated fluorographene for high-performance lithium primary batteries. *Nanoscale* **2014**, *6*, 2634–2641. [CrossRef]
39. Zhang, S.S.; Foster, D.; Read, J. Carbothermal treatment for the improved discharge performance of primary Li/CF_x battery. *J. Power Sources* **2009**, *191*, 648–652. [CrossRef]
40. Jiang, S.; Huang, P.; Lu, J.; Liu, Z. The electrochemical performance of fluorinated ketjenblack as a cathode for lithium/fluorinated carbon batteries. *RSC Adv.* **2021**, *11*, 25461–25470. [CrossRef]
41. Tressaud, A.; Moguet, F.; Flandrois, S.; Chambon, M.; Guimon, C.; Nanse, G.; Papirer, E.; Gupta, V.; Bahl, O. On the nature of C F bonds in various fluorinated carbon materials: XPS and TEM investigations. *J. Phys. Chem. Solids* **1996**, *57*, 745–751. [CrossRef]
42. Li, Y.; Feng, Y.; Feng, W. Deeply fluorinated multi-wall carbon nanotubes for high energy and power densities lithium/carbon fluorides battery. *Electrochim. Acta* **2013**, *107*, 343–349. [CrossRef]
43. Wang, J.; Sun, M.; Liu, Y.; Lin, J.; Wang, L.; Xu, Z.; Wang, W.; Yuan, Z.; Liu, J.; Bai, X. Unraveling nanoscale electrochemical dynamics of graphite fluoride by in situ electron microscopy: Key difference between lithiation and sodiation. *J. Mater. Chem. A* **2020**, *8*, 6105–6111. [CrossRef]
44. Luo, Z.; Wang, X.; Chen, D.; Chang, Q.; Xie, S.; Ma, Z.; Lei, W.; Pan, J.; Pan, Y.; Huang, J. Ultrafast Li/fluorinated graphene primary batteries with high energy density and power density. *ACS Appl. Mater. Interfaces* **2021**, *13*, 18809–18820. [CrossRef] [PubMed]
45. Dai, Y.; Fang, Y.; Cai, S.; Wu, L.; Yang, W.; Yan, H.; Xie, J.; Zheng, J.-C.; Takeuchi, E.; Zhu, Y. Surface modified pinecone shaped hierarchical structure fluorinated mesocarbon microbeads for ultrafast discharge and improved electrochemical performances. *J. Electrochem. Soc.* **2016**, *164*, A1. [CrossRef]
46. Watanabe, N. Two Types of Graphite Fluorides,$(CF)_n$ and $(C_2F)_n$, and Discharge Characteristics and Mechanisms of Electrodes of $(CF)_n$ and $(C_2F)_n$ in Lithium Batteries. *Solid State Ionics* **1980**, *1*, 87–110. [CrossRef]
47. Wang, L.; Wu, Z.; Zou, J.; Gao, P.; Niu, X.; Li, H.; Chen, L. Li-free cathode materials for high energy density lithium batteries. *Joule* **2019**, *3*, 2086–2102. [CrossRef]
48. Zhao, X.; Tu, J.; Lu, Y.; Cai, J.; Zhang, Y.; Wang, X.; Gu, C. Graphene-coated mesoporous carbon/sulfur cathode with enhanced cycling stability. *Electrochim. Acta* **2013**, *113*, 256–262. [CrossRef]
49. Dai, Y.; Cai, S.; Wu, L.; Yang, W.; Xie, J.; Wen, W.; Zheng, J.-C.; Zhu, Y. Surface modified CF_x cathode material for ultrafast discharge and high energy density. *J. Mater. Chem. A* **2014**, *2*, 20896–20901. [CrossRef]
50. Deiss, E. Spurious chemical diffusion coefficients of Li^+ in electrode materials evaluated with GITT. *Electrochim. Acta* **2005**, *50*, 2927–2932. [CrossRef]
51. Zhong, G.; Chen, H.; Cheng, Y.; Meng, L.; Liu, H.; Liu, Z.; Zheng, G.; Xiang, Y.; Liu, X.; Li, Q. Insights into the lithiation mechanism of CF_x by a joint high-resolution ^{19}F NMR, in situ TEM and ^{7}Li NMR approach. *J. Mater. Chem. A* **2019**, *7*, 19793–19799. [CrossRef]
52. Wang, L.; Li, Y.; Wang, S.; Zhou, P.; Zhao, Z.; Li, X.; Zhou, J.; Zhuo, S. Fluorinated nanographite as a cathode material for lithium primary batteries. *ChemElectroChem* **2019**, *6*, 2201–2207. [CrossRef]